Advanced Functional Materials

ADVANCED FUNCTIONAL MATERIALS
www.afm-journal.de

RESEARCH ARTICLE OPEN ACCESS

DNA-Origami-Assembled Rhodium Nanoantennas for Deep-UV Label-Free Single-Protein Detection

Nicco Corduri[1] | Malavika Kayyil Veedu[2] | Yifan Yu[3] | Yanqiu Zou[4] | Jie Liu[3] | Denis Garoli[4,5,6] | Guillermo P. Acuna[1,7] | Jérôme Wenger[2] | Karol Kołątaj[1]

[1]Department of Physics, University of Fribourg, Fribourg, Switzerland | [2]Aix Marseille Univ, CNRS, Centrale Med, Institut Fresnel, AMUTech, Marseille, France | [3]Department of Chemistry, Duke University, Durham, North Carolina, USA | [4]College of Optical and Electronic Technology, China Jiliang University, Hangzhou, China | [5]Optoelectronics, Istituto Italiano di Tecnologia, Genova, Italy | [6]Dipartimento Di Scienze e Metodi Dell'ingegneria, Università di Modena e Reggio Emilia, Via Amendola 2 Padiglione Tamburini, Reggio Emilia, Italy | [7]Swiss National Center For Competence in Research (NCCR) Bio-inspired Materials, University of Fribourg, Fribourg, Switzerland

Correspondence: Denis Garoli (denis.garoli@unimore.it) | Guillermo P. Acuna (guillermo.acuna@unifr.ch) | Jérôme Wenger (jerome.wenger@fresnel.fr) | Karol Kołątaj (karol.kolataj@unifr.ch)

Received: 2 December 2025 | **Revised:** 16 February 2026 | **Accepted:** 9 March 2026

Keywords: deep UV | DNA origami | label-free single molecule detection | plasmonics | rhodium nanocubes | single molecule fluorescence

ABSTRACT

Plasmonic metal nanoparticles have deeply impacted the spectroscopy field by enabling nanoscale concentration of light and powerful signal enhancement. However, their operation remains largely confined to the visible and near-infrared spectral ranges due to the poor stability and limited surface functionalization strategies of UV-active materials. Here, we establish a complete route for the fabrication of programmable UV-plasmonic nanoantennas based on rhodium nanocube dimers assembled on DNA origami scaffolds. We report on an effective surface ligand exchange protocol for functionalizing rhodium nanocubes with DNA strands enabling their assemble into dimers with a yield of 69%, and an interparticle distance of 10 nm. Thanks to the DNA origami, a single streptavidin protein is accurately positioned into the plasmonic nanogap, contrasting to other works relying only on random diffusion. In good agreement with numerical simulations, UV autofluorescence measurements on a single streptavidin indicate up to 22× brightness enhancement factor with the average value of 6.6×, shorter autofluorescence lifetimes, and over 10× increase of the total photon budget. By pioneering a robust, versatile and selective strategy for constructing UV-resonant plasmonic nanoantennas, this work broadens the applications of plasmonics into the deep UV range and opens new opportunities for label-free spectroscopy of single proteins.

1 | Introduction

The ability of plasmonic metal nanoparticles (NPs) to concentrate the electromagnetic field at the nanoscale has been widely exploited for enhanced spectroscopy techniques such as surface-enhanced Raman scattering (SERS), fluorescence, and circular dichroism [1–3]. However, unlocking the optical potential of plasmonic NPs into practical plasmonic-enhanced spectroscopy tools requires a careful consideration for the NP assembly and their surface functionalization [4, 5]. A particularly effective strategy is to graft the surface of NPs with a monolayer of thiol-terminated single-stranded DNA (ssDNA) forming strong sulfur bonds to the metal [6–8]. Such DNA shells not only stabilize the NPs in high-salt media but also encode sequence-specific recognition, transforming the NPs into uniquely addressable, programmable building blocks [8]. DNA origami is a highly adaptable bottom-up technique that makes full use of DNA's programmable nature, enabling the precise placement of nanoparticles and

other components (such as fluorophores, quantum dots, proteins, enzymes, or nucleic acids) with nanometer-level accuracy and exact stoichiometric control down to individual molecules [9, 10] This deterministic placement fully leverages the optical properties of plasmonic NPs and enables reproducible enhancement of fluorescence and SERS down to the single molecule level [11, 12].

To date, DNA functionalization has been realized predominantly for Au and Ag NPs with some excursions into high refractive index materials [13, 14]. Thus, DNA and DNA origami–based plasmonic systems operate almost exclusively in the visible/near-IR [9, 11]. However, this spectral range misses the many opportunities open in the ultraviolet (UV) where molecular absorption is the highest, notably the π–π^* bands of aromatic amino acid residues such as tryptophan [15–22]. Extending the operating range of origami-based plasmonic nanoantennas toward the deep-UV unlocks the key benefit to probe directly the protein intrinsic UV autofluorescence and avoids the need for additional fluorescence labeling [23–31]. Moreover, the deep UV range enables the exploitation of resonance enhancement in SERS, where spectral overlap between the plasmonic mode and molecular absorption bands leads to significantly amplified signals [21, 32–37]. DNA origami-based nanoantennas provide the supplementary crucial advantage of accurately localizing the protein target inside the antenna nanogap hotspot with nanometer and stoichiometric control [10, 38–40]. So far, the earlier works on UV plasmonic antennas relied on nonspecific deposition of dense molecular layers [32–35, 41–46], or random translational diffusion into the hotspot area [31, 47, 48], but DNA origami antennas and their high potential to deterministically locate a single target emitter into the hotspot remain unexplored in the deep UV range.

Beyond the visible, a subset of materials, most notably Al, Ga, Mg, and Rh, supports localized surface plasmon resonances in the UV range [17, 20, 49–52]. However, despite a decade of synthetic advances that yield diverse shapes and sizes of UV-active NPs, their practical application remains strongly limited by their surface chemistry and stability [53–56]. Al, Mg, and Ga are highly reactive, with large oxidation enthalpies [49]. While stable in organic solvents, they therefore tend to oxidize in aqueous environments [53, 57]. Their stability could be increased by depositing a dielectric coating [53, 58], yet this coating substantially dampens the near field intensity enhancement and reduces the spectroscopic performance [59, 60]. To overcome these limitations, rhodium stands out as a particularly promising material for UV plasmonics combining strong UV resonances with high chemical stability [36, 61–66]. However, most of the UV-active Rh NPs such as nanocubes (NC) or tripods are synthesized using organic polyol routes in the presence of polyvinylpyrrolidone (PVP) molecules. This ligand protects the growing crystals and steers their morphology to ensure high reproducibility of their size and shape [61–63]. At the same time, PVP binds so efficiently and densely to the metal surface that it blocks its surface to the interaction with other molecules, thus hindering the functionalization. Consequently, the colloidal functionalization of Rh NPs with DNA has not been achieved so far. Establishing a robust method of removing PVP from Rh surface and their subsequent DNA functionalization would unlock the fabrication route of programmable UV nanoantennas with deterministic analyte placement, expanding plasmon-enhanced fluorescence and resonant SERS into the deep-UV regime where light-molecule interaction is the strongest.

In this work, we pioneer a route for integrating UV-active plasmonics together with DNA origami nanotechnology. Our first major result is a reliable strategy for functionalizing Rh NCs with DNA strands, which involves a dedicated approach to remove the PVP ligands from the Rh surface. Second, using the DNA origami scaffold, we assemble well-defined UV-resonant Rh dimer antennas in a face-to-face configuration, achieving an average interparticle distance of 10 nm and a yield of 69%. A single streptavidin protein is deterministically positioned into the plasmonic nanogap, contrasting to earlier works relying only on random diffusion [30, 47, 48]. The UV autofluorescence intensity recorded from the streptavidin protein inside the hotspot indicate an average enhancement of 6.6× as compared to the reference on quartz, together with a 6.6× reduction of the autofluorescence lifetime and a 10× increase of the total photon budget. The experimental results are in very good agreement with numerical simulations, highlighting the high nanofabrication and positioning accuracy enabled by our UV-active nanoantennas. By establishing a robust and versatile strategy for the realization of UV-resonant Rh nanoantennas, our work broadens the applicability of plasmonics down into the deep UV range and paves the way toward enhanced label-free spectroscopy with single molecule resolution [16, 23, 67, 68].

2 | Results and Discussion

Rhodium NCs with a side length of 23.6 ± 1.9 nm are selected as a model UV-plasmonic system for their strong localized surface plasmon resonances (LSPRs) in the UV range and their excellent chemical stability in aqueous environments [63]. Transmission electron microscopy (TEM) images shown in Figure S1a,b confirms the successful synthesis using the polyol method (see Methods section for details about the Rh NCs synthesis protocol).

To construct programmable UV-plasmonic Rh nanoantennas on DNA origami scaffolds, we need to establish an efficient ligand-exchange process that preserves colloidal stability and enables functionalization of the Rh surface with DNA. Our dedicated surface modification protocol involves two steps: first, we remove the PVP ligand bound to the metal surface, and then we introduce thiolated single-stranded DNA (ssDNA), as shown schematically in Figure 1a. The PVP binding mechanism is based on the formation of coordination bonds between the Rh atoms and the carbonyl oxygen of the PVP molecules (Figure 1b). To expose the metal surface for interaction with DNA, we use sodium borohydride ($NaBH_4$) to reduce the coordination bonds and compete with the PVP molecules, removing them from the NCs. However, $NaBH_4$ is a strong reducing agent that can destabilize colloids and cause their aggregation. Therefore, the process was carefully optimized to be carried out at low temperature, assisted by sonication to minimize aggregation, and then stabilized by adding the competing surfactant (Pluronic F-127) to replace the detached PVP molecules (see the Materials and Methods section for details). After PVP removal, the NCs are functionalized with thiolated poly-thymine (poly(T)18) DNA strands routinely used for the functionalization of metallic NPs. Functionalization is

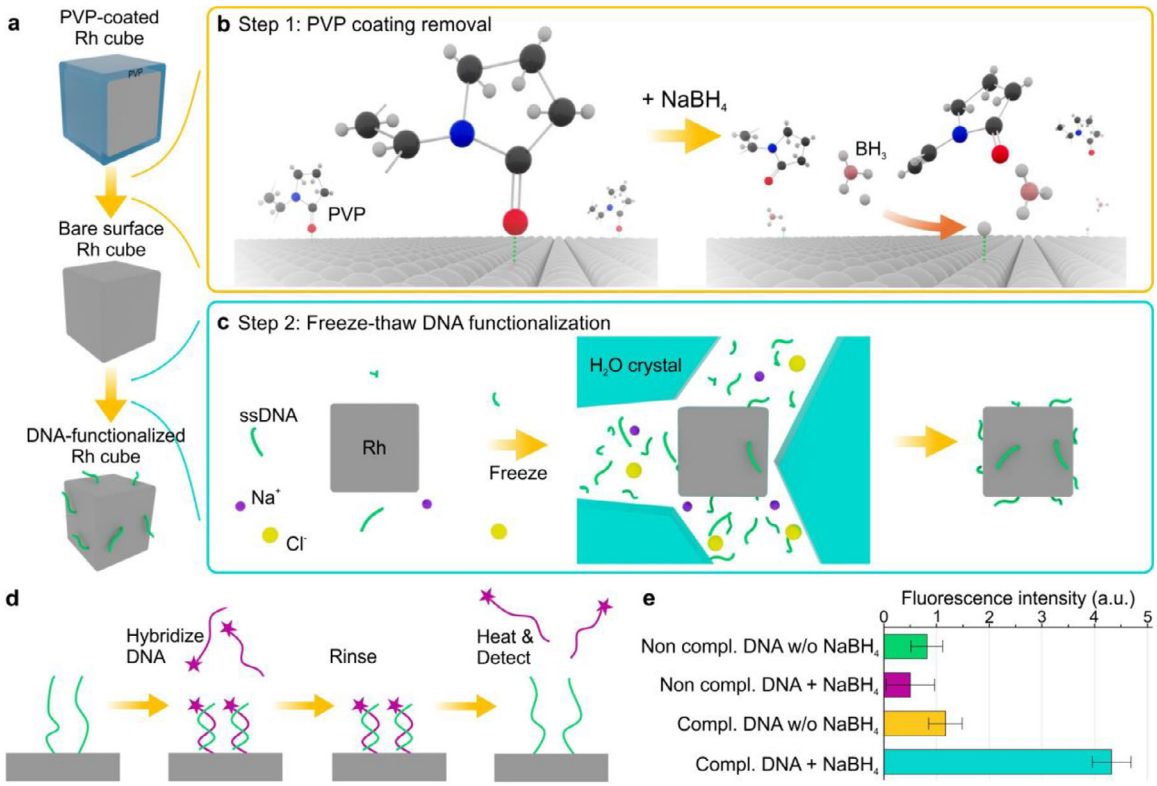

FIGURE 1 | Surface functionalization of Rh NCs with single-stranded DNA. (a) Full workflow of the DNA functionalization of Rh NCs. (b) Mechanism of PVP removal from Rh NCs by $NaBH_4$ through cleaving Rh-carbonyl bond. (c) Schematic representation of the NC surface functionalization with DNA using the "Freeze–thaw" method. (d) Workflow of the fluorescence assay used to quantify DNA attachment on the Rh NCs. (e) Fluorescence intensity measurements for Rh NCs with and without PVP coating incubated with either a complementary or a non-complementary DNA strand labeled with the fluorescent dye ATTO 647N.

performed using a "Freeze–thaw" method, in which the freezing step promotes efficient binding between the metal and thiolated DNA, as shown in Figure 1c [69].

To assess the performance of our Rh surface functionalization protocol, we use a fluorescence assay whose principle is summarized in Figure 1d. The assay relies on the specific hybridization of the fluorophore-labeled DNA strands (Poly(A)18 – ATTO 647N) complementary to the poly(T)18 DNA strands on the NC surface. After hybridization and washing, the fluorescence from the surface-hybridized strands is measured. A strong fluorescence signal is observed only for the complementary DNA strands using the NCs treated with $NaBH_4$ (Figure 1e). On the contrary, untreated Rh NCs samples retaining the surface PVP ligands show only weak nonspecific emission comparable to that observed when a non-complementary DNA sequence is used. These results confirm the successful surface functionalization of Rh NCs with specific thiolated DNA strands, highlighting that PVP removal represents a critical step to enable DNA functionalization. From the fluorescence intensity in Figure 1e, we estimate the surface density of DNA to be approximately 0.05 molecules nm^{-2}, consistent with the densities reported for Ag NCs [70]. Gel electrophoresis confirms our results (Figure S1c), where only NCs functionalized after PVP removal migrated through the gel, indicating successful DNA conjugation and increased surface charge. Additionally, as can be seen from the gel analysis in Figure S1d,e, DNA functionalization combined with gel electrophoresis enables for the separation between the different fractions formed during the NCs. This step is crucial, as it allows the selection of well-defined nanoparticles suitable for subsequent optical applications.

Having achieved a reliable surface functionalization of the Rh NCs with DNA, we now use DNA origami scaffolds to assemble the NCs into well-defined plasmonic nanogap antennas designed to enhance the UV autofluorescence of native proteins (Figure 2a). The rectangular base of our DNA origami template features a length of 180 nm, a width of 15 nm and a height of 5 nm. It includes a "mast" of 8.5 nm width and 20 nm height placed in the center (Figure S2) [14, 71]. A single biotin extension is added at the top of the mast to precisely bind a single streptavidin protein and locate it inside the plasmonic hotspot. We check the binding of streptavidin to the DNA origami by fluorescence microscopy as shown in Figure S3. To attach the Rh NCs to the DNA scaffold, the origami features 32 poly(A)8 handles complementary to the poly(T)18 DNA on the NC surface. Half of the hybridization handles protrude from the base, with the other half protruding from the mast. This design ensures specific and reproducible Rh NC dimer formation while leaving the hotspot area accessible to the target molecule [72]. To ensure high quality of the sample used for the fluorescence measurements, the obtained dimers were separated from the excess of Rh NCs after binding via the gel electrophoresis, as presented in Figure S4. Transmission electron microscopy confirms the formation of well-aligned dimers with an average interparticle distance of 10.7 ± 3.2 nm and a yield of 69% (Figure 2b,c).

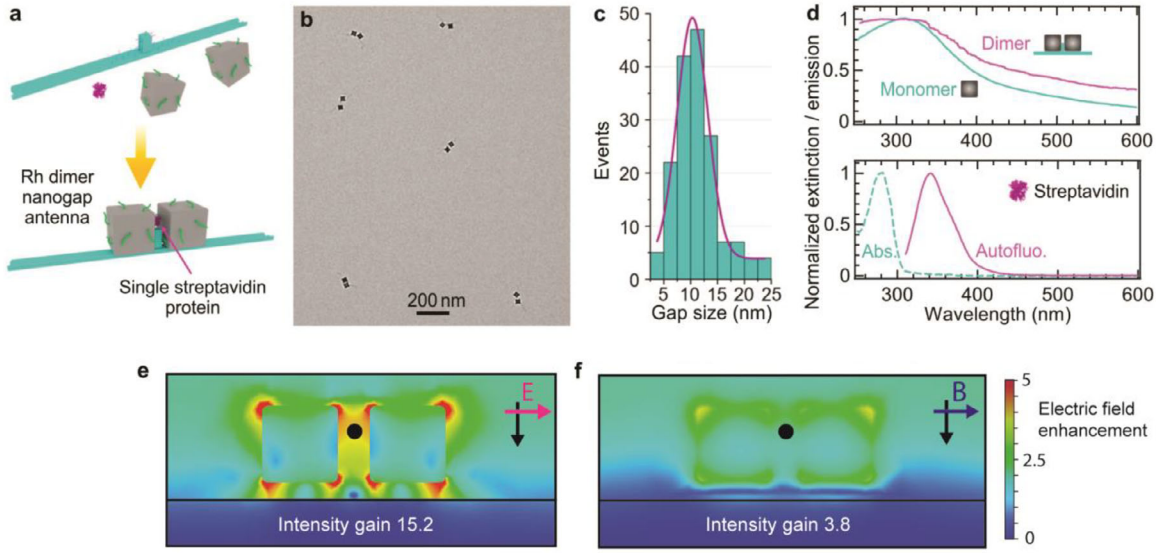

FIGURE 2 | Deep-UV self-assembled plasmonic nanoantennas. (a) Realization of a UV nanoantenna composed of a Rh NC dimer with a single streptavidin precisely positioned in the hotspot via a DNA origami scaffold. (b) TEM image of 24 nm Rh NC dimer antennas. (c) Gap size distribution obtained from TEM images out of 164 individual dimer antennas. (d) Normalized extinction spectra of the Rh dimer antenna and single Rh NCs, together with the normalized absorbance and autofluorescence emission of a 12 μM streptavidin solution. All spectra were acquired in solution using a NanoDrop UV–vis spectrophotometer. (e,f) Distribution of the electric field enhancement around a Rh dimer nanoantenna with 10 nm gap under linearly polarized light at 266 nm with the electric field (e) parallel and (f) perpendicular to the dimer main axis. The excitation intensity gain indicated at the bottom corresponds to the streptavidin position (black dot marker).

The extinction spectrum of the Rh NCs dimer in solution shows a plasmonic resonance at 320 nm, slightly red-shifted as compared to the plasmon band of the Rh NC monomer (Figure 2d). Importantly, the plasmon resonance of the dimers is in good agreement with the simulated optical properties (Figure S5) and still overlaps with the absorption and emission band of streptavidin in the UV (Figure 2d), indicating the strong UV activity of Rh NCs make them relevant candidates for UV-enhanced spectroscopy.

To evaluate the antenna near-field distribution under 266 nm illumination, consistent with our experimental excitation wavelength, we perform numerical simulations on a Rh dimer with 24 nm side length and 10 nm gap corresponding to the experimental conditions (Figure 2e,f). The Rh NCs antenna is placed above an Al mirror to further increase the excitation and emission gains [73, 74], with a 5.5 nm spacing corresponding to the thickness of the DNA origami. Far-field simulations (Figure S5) indicate that placing the Rh NC dimer on the Al mirror has little impact on the optical response, preserving the overlap between the surface plasmon resonance and the molecular electronic transition. Additionally, the near-field amplitude maps in Figure 2e,f show that the dimer behaves like an efficient optical nanogap antenna, concentrating the electric field inside the gap and demonstrating a polarization-sensitive response. When the incoming field polarization aligns with the dimer main axis (Figure 2e), the plasmonic coupling leads to a strong electromagnetic confinement with a 15.2× amplification of the local excitation intensity. When the illumination polarization is rotated by 90° (Figure 2f), the coupling decreases and the intensity gain is reduced by approximately 4 times.

We also tested numerically whether small angular misalignments of the NCs in the dimer could affect the antenna's performance. To our surprise, the simulations shown in Figure S6 indicate a moderate impact of NCs angling (from 0.5 to 2.5×) on the fluorescence enhancement compared to the perfectly formed face-to-face dimers, indicating that our UV nanoantennas are quite robust to minor geometric deviations without loss of performance. Finally, we investigated the influence of the Rh NC size on the resulting fluorescence enhancement in the dimer. To obtain general insights into the system performance, the dipole was placed at the exact geometrical center of the dimer, rather than at the position dictated by the DNA origami design used in the experiments. The results shown in Figure S7 indicate that the highest fluorescence intensity at 350 nm is achieved for 25 nm Rh NCs. For both smaller and bigger nanoparticles the fluorescence enhancement is reduced due to decreased electric field in the gap, as well as smaller quantum yield enhancement. These findings rationalize the choice of 24 nm NCs for optical measurements.

Figure 3 summarizes our main experimental findings monitoring the autofluorescence of single streptavidin proteins located inside the plasmonic hotspot of Rh NCs dimer antenna. The origami structures with or without streptavidin are dispersed on an aluminum mirror and scanned individually with a UV confocal microscope with 266 nm laser illumination and autofluorescence detection in the 310–410 nm range (Figure 3a). Confocal scans in presence of the Rh nanoantennas loaded with streptavidin show distinct bright spots, which we associate to the nanoantenna signal (Figure S9). To ensure the specificity and origin of the detected fluorescence signal, we employed multiple lines of evidence. First, the detection of autofluorescence in the presence of streptavidin, combined with a low background signal in its absence (Figure 3b; Figure S8), strongly indicates that the observed signal originates from the protein within the nanogap. Second, our experimental observations are well supported by numerical

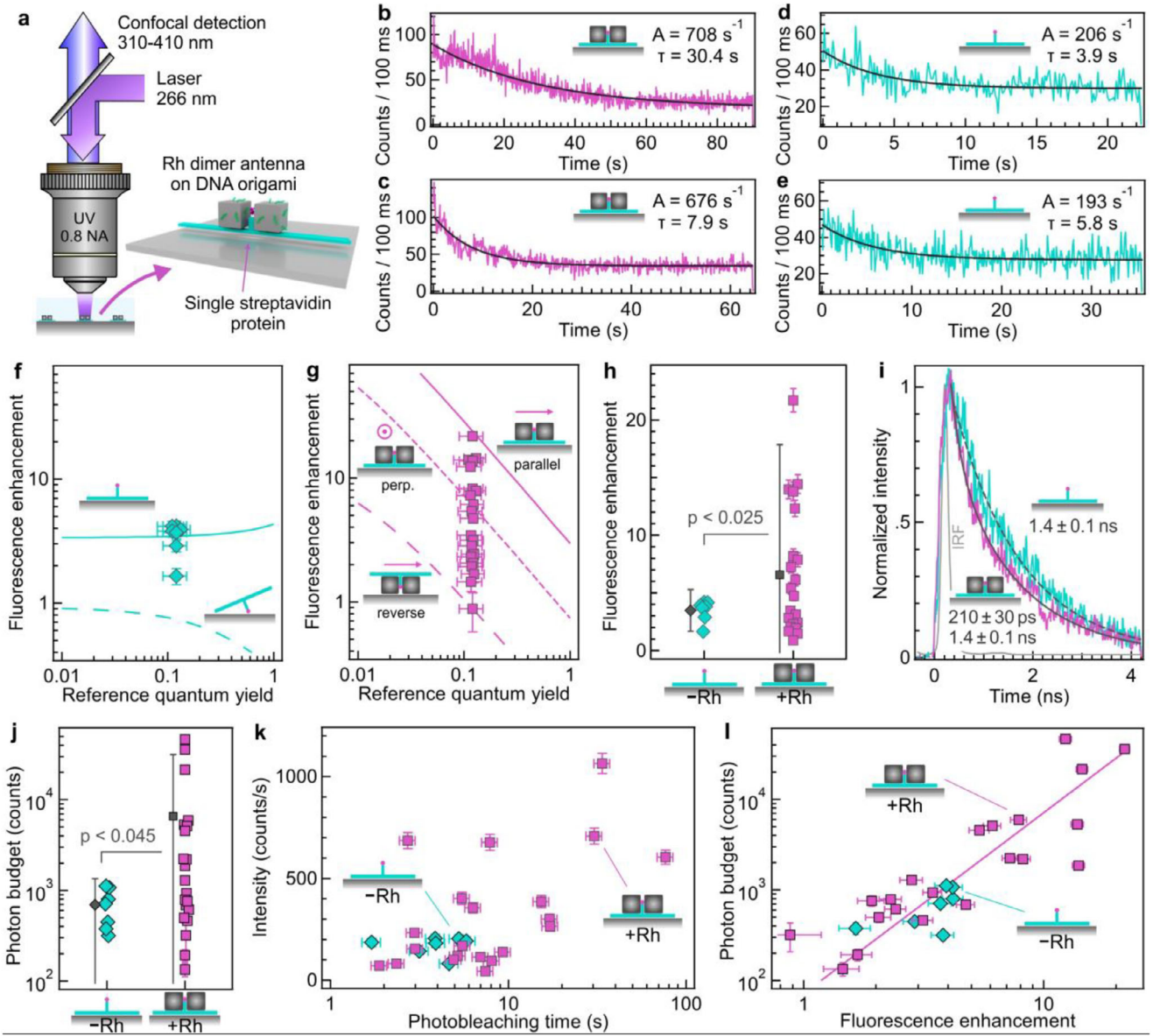

FIGURE 3 | Label-free single-protein detection with plasmonic-enhanced deep-UV autofluorescence. (a) Scheme of the experimental setup. (b–e) Representative autofluorescence time traces recorded for a single streptavidin protein localized on a DNA origami in presence (b,c) or absence (d,e) of the Rh NCs antenna. The autofluorescence traces are fitted with a single exponential decay (thick black line) with the respective amplitude A and decay time τ indicated on each graph. Supplementary traces are shown in Figure S8. (f,g) Fluorescence enhancement factors as a function of the reference quantum yield in homogeneous solution environment. The markers correspond to the experimental data in absence (f) or presence (g) of the Rh NCs antenna. The presentation of the experimental data includes some random shift along the *x*-axis to better view the different points. The solid lines in (f) correspond to numerical simulations when the DNA origami base is in contact with the aluminum mirror while the dashed lines denote the simulations results where the origami position is reversed respective to the mirror, and the streptavidin is at the closest distance to the mirror. The dotted line in (g) corresponds to numerical simulations when the DNA origami base is in contact with the Al mirror and the polarization is perpendicular to the dimer main axis. (h) Comparison of the fluorescence enhancement factors in absence or presence of the Rh NCs antenna. The black markers indicate the average value with the error bars corresponding to 2× the standard deviation. The error bars on the individual data points correspond to the experimental uncertainties, which appear in some cases smaller than the marker size. The p-values written on the graphs result from statistical *t*-tests performed on the distributions. (i) Normalized time-resolved decay traces measured in absence or presence of the Rh NCs antenna, cumulated over the 5 brightest systems of each case. The same data is shown in logarithmic scale in Figure S11b. IRF indicates the instrument response function. (j) Comparison of the total photon budgets. (k) Scatter plot of the autofluorescence decay amplitude versus the photobleaching time. (l) Scatter plot of the total photon budget versus the autofluorescence enhancement factor confirming the gain brought by the brightest antennas. The line is an empirical fit following a quadratic dependence.

simulations, as we discuss further below. Third, the binding tests reported in Figure S3 confirm the specific interaction between streptavidin and biotin and validate the presence of streptavidin on the DNA origami. Finally, recent surface-enhanced Raman scattering (SERS) experiments performed on similar RhNC–DNA origami–single streptavidin constructs confirm the precise positioning of the protein within the nanogap [75].

Figure 3b–e presents typical autofluorescence time traces recorded for a single streptavidin protein localized on a DNA origami in presence or absence of the Rh NCs antenna. Supplementary traces are shown in Figure S8. Contrarily to the stepwise photobleaching of a single organic fluorophore [39], each streptavidin molecule contains 24 tryptophan and 24 tyrosine residues that bleach sequentially with overlapping decay steps, resulting in an overall exponential-like fluorescence decay. Unfortunately, the signal to noise ratio is not sufficient to unequivocally distinguish the photobleaching steps from individual amino acids. Therefore, the autofluorescence time trace of each detected streptavidin is fitted with a single exponential decay to extract the autofluorescence amplitude A and decay time τ. To assess the reliability of our numerical analysis and the influence of low signal-to-noise conditions, we simulate autofluorescence traces with known amplitudes, decay times, and noise comparable to the experiments (Figure S10). The fitting procedure accurately retrieves the input parameters down to amplitudes of 80 counts/s, confirming the robustness of the experimental measurements reported in Figure 3.

To promote the photostability and reduce the bleaching time, we have to lower the 266 nm laser power down to 220 nW. In such conditions, measuring the reference emission from a single streptavidin protein on a reference quartz coverslip is extremely challenging (amplitude estimated to less than 50 photons/s). Instead, we rely on the measurements recorded on the DNA origami with a single streptavidin on an Al mirror in absence of the Rh NCs dimer and compare the average amplitude with the numerical prediction of the 3.5× autofluorescence enhancement in the sole presence of the aluminum mirror (Figure 3f). This allows us to indirectly assess the reference signal for streptavidin on a quartz substrate used to compute the fluorescence enhancement factors in Figure 3. The simulations in Figure 3f consider two main orientations for the DNA origami structure either lying flat on the surface (maximum 26 nm distance between the streptavidin and the Al surface) or reverse (streptavidin in direct contact with the Al metal, leading to maximum autofluorescence quenching). The influence of the quantum yield of the emitter and the collection efficiency are also taken into account as parameters. While the quantum yield of each aromatic residue in the protein is not known, we base our calculations on the 12% reference found for tryptophan and tyrosine [15, 76], and add a ± 3% uncertainty on the *x*-axis error bars together with a random ± 1% shift along the *x*-axis to better visualize the different data points, as seen in Figure 3f.

The results presented in Figure 3g demonstrate that the UV autofluorescence of streptavidin is significantly enhanced in the presence of the Rh NC antenna as compared to the quartz reference, with a maximum value of 22×. This enhancement aligns with the maximum predicted value of 24×, which arises from a combination of increased excitation intensity, moderate quantum yield quenching and improved photon collection, as detailed in Table S1. However, the experimental data exhibits a broad distribution, with several antennas with enhancement factors below 2.5×, leading to an average enhancement of 6.6×. We attribute the variability in presence of the Rh NCs to differences in the orientation of the DNA origami relative to the aluminum mirror (either "up-oriented" or "reversed") and the polarization of the incoming laser. Due to the relatively short photobleaching times, we were unable to rotate the linear polarization of the laser during measurements. As a result, each Rh NC antenna was exposed to a fixed, random polarization orientation, contributing to the observed dispersion in signal intensity. While comparing the Rh NC antennas to the autofluorescence signal on the Al surface alone, the average gain brought by the Rh NCs is hence relatively modest, with a 1.8× increase in autofluorescence (Figure 3h).

To rationalize these experimental findings, we examined the influence of key experimental parameters, including the orientation of the DNA origami or Rh NC dimers on the Al surface and the laser polarization. We considered two probable configurations for the DNA origami: an "up-oriented" configuration, where the structure lies flat on the Al surface, and a "reverse" inverted configuration, where the streptavidin is positioned close to the surface. Since the exact conformation of each structure cannot be experimentally determined, our analysis relies on numerical simulations, whose main results are summarized in Table S1.

The simulations results for Rh NC dimers shown in Figure 3g exhibit a broad signal distribution, ranging between the calculated enhancement values of 24× for "up-oriented" dimers and 0.97× for "reverse" orientation. In the latter case, the quantum efficiency is reduced tenfold to 1.2%, and the excitation gain drops to 4.4×. Additionally, as previously discussed and illustrated in Figure 2e,f, the fluorescence enhancement of Rh NC dimers is highly dependent on the excitation polarization. Misalignment between the laser polarization and the dimer orientation further modifies the signal intensity. Our simulations reveal that, for laser polarization perpendicular to the dimer's main axis, the expected fluorescence enhancement decreases to 5.9× and 0.037× for "up-oriented" and "reverse" dimers, respectively.

Taking into account both the dimer orientation and the laser polarization dependence, we calculate an average fluorescence enhancement of 7.7× for Rh NC dimers on Al relative to free streptavidin on quartz, corresponding to a 2.0× enhancement compared to the Al surface alone. Experimentally, we obtain average values of 6.6× relative to the quartz reference, and 1.8× compared to the Al surface. The close agreement between the simulated and measured enhancements validates our experimental observations and underscores the reliability of DNA-guided assembly for precisely positioning the protein within the plasmonic hotspot. These findings also highlight the importance of precise control over deposition geometry and alignment of the dimers with respect to the excitation polarization for achieving optimal performance [48, 77, 78].

Some of our earlier work used capillary-assembled Rh NCs into rectangular nanoholes to enhance the UV autofluorescence of freely diffusing proteins [48]. While this platform achieved autofluorescence enhancement factors of 50–70× for the

best-performing nanoantennas, it relied entirely on the random diffusion of proteins into the nanogap, resulting in significant signal fluctuations and limited positional control. For further comparison, the non-resonant UV horn antenna design achieved an autofluorescence enhancement of 8.3× for diffusing streptavidin proteins [47]. High laser power up to 30 μW were used, but the occurrence of photobleaching was not considered in these earlier works. Additionally, complex data processing, including fluorescence correlation spectroscopy (FCS) and background removal, was required to isolate the nanogap signal from background autofluorescence. In contrast, our approach uses DNA-guided positioning to achieve deterministic control of the location of both nanoparticles and analytes, thereby achieving a highly specific optical response with a true control on the positioning and number of target protein. This method not only eliminates the stochastic limitations of diffusion-based systems, it also ensures a well-defined experimental reference with straightforward data analysis, thereby offering a robust platform for single-molecule UV plasmonics.

Measuring the autofluorescence lifetime from a single immobilized protein is difficult as the limited photon budget is split across the different photon delay times. By summing up the signal from 5 different proteins, we could nevertheless obtain relevant lifetime histograms in presence or absence of the Rh NCs antenna (Figure 3i). Without the Rh antenna, the 1.4 ns autofluorescence lifetime in the vicinity of the Al mirror remains comparable to the reference value measured for a 1 μM streptavidin solution (Figure S11a,b), in good agreement with the numerical predictions (Figure S11c). Thanks to the plasmonic enhancement inside the nanogap antenna, the autofluorescence lifetime is shorter in presence of the Rh NCs. Our measurements indicate a 210 ± 30 ps component corresponding to a 6.6× lifetime reduction. The numerical simulations predict even higher lifetime reductions up to 10 or 25× depending on the DNA origami orientation (Figure S11c). Despite this discrepancy, the overall trend is preserved, confirming the plasmonic enhancement of the total decay rate [39]. It should also be mentioned that the spectroscopy experiments average over 24 different tryptophan and tyrosine residues with varying positions and orientations while our numerical model only accounts for a single dipole located in the center of the nanogap with a constant parallel orientation.

The lifetime measurements in Figure 3i reveal that 28% of the total amplitude arise from a short-lived component (210 ps), corresponding to emitters strongly coupled to the nanogap, while 72% stem from a longer-lived component (1.4 ns). This long lifetime component reflects the intricate photodynamics of streptavidin, which contains 24 tryptophan and tyrosine residues that can engage in Förster resonance energy transfer (FRET) [79]. Donor dipoles aligned parallel to the nanogap are preferentially excited and decay rapidly, but they can transfer energy to less coupled acceptors oriented perpendicularly, resulting in delayed emission and an apparent longer lifetime. Although this long-lived component might seem counterintuitive, it still contributes to the overall brightness enhancement, as the weakly coupled acceptors can still be excited more efficiently through donor-mediated energy transfer [80].

The photon budget defined as the total number of photons detected before photobleaching is a crucial parameter for single molecule fluorescence experiments [81, 82]. For a single exponential bleaching decay, the photon budget corresponds to the product $A^*\tau$ of the amplitude by the photobleaching decay time. Figure 3j compares the distributions of the photon budgets for the different detected proteins. In presence of the Rh NCs antenna, the average photon budget is increased by a factor of 9.4 from 700 to 6600. This results from the enhancement of the autofluorescence amplitude A (Figure 3h) and also to some increase in the photobleaching time τ (Figure 3k). As already observed for organic fluorescent dyes in the visible [82, 83], the photobleaching time follows a broad distribution covering multiple orders of magnitude (Figure 3k). In presence of the nanoantenna, the higher excitation intensity will tend to reduce τ, yet this effect can be partially compensated by the reduced autofluorescence lifetime limiting the time spent in the higher excited state leading to photo-oxidation and bleaching [84, 85]. Altogether, Figure 3l summarizes the performance comparison between DNA origami structures with and without the Rh NCs, considering both fluorescence enhancement and total photon budget. Likely due to variations in orientation relative to the laser polarization and/or the aluminum mirror, some Rh NC antennas exhibit responses similar to the reference DNA origami alone. However, a distinct population showing approximately 10× higher fluorescence intensity and 10× higher photon budget clearly demonstrates the superior performance of the UV plasmonic antennas.

To further increase the autofluorescence enhancement, we have performed numerical simulations for other Rh NC dimers configurations. Specifically, we analyzed edge-to-edge and tip-to-tip configurations, in addition to the experimentally realized face-to-face configuration that are presented in Figure S12. The alternative designs showed even stronger field enhancement in the hotspots, with near-field intensity gains of 25× and 36× compared to 15.2× for the original geometry, which is related to a better plasmonic optical confinement in these cases. After considering the gains in quantum yield and collection efficiency, the overall fluorescence enhancement for parallel polarization reached 47× and 69× for edge-to-edge and tip-to-tip dimers, as compared to the free emitter. Looking at the reference on an Al mirror, the net autofluorescence gains become 12× and 18×. These results suggest that further adjustment of the dimer geometry using DNA origami can greatly enhance their performance as UV nanoantennas. However, the synthesis of such variants is beyond the scope of this study, which focused on establishing a fabrication pathway for a new class of UV plasmonic nanoantennas rather than investigating several different configurations of NPs to maximize the performance.

3 | Conclusions

In this work, we establish a complete route for transforming Rh NCs into programmable UV-plasmonic nanoantennas through surface-specific functionalization. To this end, we report an effective method for removing the native PVP ligand without compromising colloidal integrity of Rh NCs, followed by their functionalization with thiolated DNA strands using a 'freeze-thaw' method. Exploiting the DNA origami technique as an addressable scaffold, we demonstrate deterministic assembly of Rh NC dimers with an average interparticle distance of 10 nm

and a yield of 69%. A single streptavidin protein is precisely positioned within the plasmonic hotspot, pioneering a route for single label-free single protein sensors enhanced with UV plasmonics. Importantly, owing to its addressability, the DNA origami technique introduces molecular selectivity, unlike previously reported UV-plasmonic systems in which analytes diffused randomly during the measurements.

UV autofluorescence measurements of single immobilized streptavidins show an average brightness enhancement factors up to 6.6× compared to the reference on quartz with the highest enhancement of 22× for perfectly aligned structures, together with a 6.6× reduction of the autofluorescence lifetime and a 10× increase of the average total photon budget. The good agreement between our experimental results and numerical simulations confirm the validity of our conclusions and highlight the remarkable nanofabrication and positioning accuracy enabled by DNA origami templated Rh nanoantennas. Overall, this work demonstrates a versatile, reproducible, and highly specific platform for constructing UV-resonant plasmonic nanoantennas, opening new opportunities for optical studies of individual label-free biomolecules in aqueous solutions. Future optimization of nanoparticle geometry and dimer orientation promises increased performance for UV-active nanoantennas and their further applications, for example in assessing the number of tryptophan and tyrosine residues.

4 | Materials and Methods

4.1 | Rhodium Cubes Synthesis

The synthesis was carried out by the polyol method developed by Zhang et al. [63]. Potassium bromide (0.45 mmol, Acros) and ethylene glycol (EG, 2 mL, J.T. Baker) were added to a 20 mL vial pre-cleaned with detergent and deionized water and dried in a vacuum oven at 80°C. The vial, equipped with a Teflon-coated magnetic stir bar, was placed in an oil bath and heated to 160°C for 40 min with the cap loosely fitted. In parallel, rhodium(III) chloride hydrate (0.06 mmol, $RhCl_3{\cdot}xH_2O$, 38% Rh, Pressure) and polyvinylpyrrolidone (PVP, 0.225 mmol in repeating units, M.W. ≈ 55 000, Aldrich) were each dissolved in 2 mL EG at room temperature. The two solutions were then simultaneously introduced into the reaction vial using a dual-channel syringe pump at 1 mL h^{-1}. Following injection, the reaction was maintained at 160°C for an additional 10 min before being cooled to room temperature.

0.4 mL of above solution was used as the seed solution and diluted with 1.6 mL EG in a cleaned 20 mL glass vial. The mixture was heated at 160°C under stirring for 40 min with the cap loosely fitted. Separately, 0.045 mmol $RhCl_3{\cdot}xH_2O$ was dissolved in 2 mL EG. 0.225 mmol PVP and 0.45 mmol KBr were co-dissolved in another 2 mL EG. These two solutions were simultaneously injected into the seed solution by a syringe pump at a rate of 1 mL h^{-1}. The reaction was kept at 160°C for another 10 min and subsequently cooled to room temperature. Rh NCs of two populations of sizes with an average edge length of 24 and 40 nm were synthesized in this way, as shown in Figure S1a,b.

Following synthesis, the reaction mixtures were washed three times with 0.5 mL deionized water and 25 mL acetone. The obtained Rh NCs were finally dispersed in 3 mL deionized water for further treatment.

4.2 | Removal of the PVP Layer on Rhodium Cubes

The removal of the PVP was carried out using a modified procedure described by Zhang et al. [86]. First, a solution of 625 pM Rh NCs, 0.1% SDS was centrifuged at 20 000 g for 12 min to remove the PVP excess from Rh NC solution. The pellet was redispersed in Milli-Q water to reach a concentration of 3.1 nM of Rh NCs and was briefly sonicated. At the same time a solution of 60 mg/mL of $NaBH_4$ was prepared with a 1:1 ratio of Milli-Q water and ethanol. The solution of Rh NCs and the $NaBH_4$ were mixed with the ratio of 1:1, followed by the addition of Pluronic F-127 to reach a concentration of 0.3%. The solution was then sonicated in a cold bath for 120 min. Afterward to stop the reaction, the solution was rinsed via centrifugation at 16 000 g for 5 min. The supernatant was removed, and the pellet was redispersed in 0.2% SDS and briefly sonicated.

4.3 | Rhodium Cubes Functionalization

400 µL of freshly PVP-removed Rh NCs (~6 nM) were mixed with 160 µL of 200 µM T18 thiolated DNA and 12 µL of 1 M NaCl. After mixing, the solution was directly frozen at −20°C. After 2 h the solution was sonicated at room temperature for 5 min to unfreeze the solution. The solution was centrifuged at 16 000 g for 5 min and the pellet was redispersed in 0.2% SDS to reach a volume of ~50 µL. Afterward the NCs were purified from the excess of DNA using 1% gel electrophoresis at 70 V and 1x TAE 12 mM $MgCl_2$ buffer. The band containing Rh NCs was cut out and extracted from the gel.

4.4 | DNA Origami Synthesis

A 7249-nucleotide-long scaffold extracted from the M13mp18 bacteriophage was folded into the desired shape using 243 staples in 1xTAE, 12 mm $MgCl_2$, pH 8 buffer. It was mixed in a 10-fold excess of staples over scaffold, and 100-fold for the functional staples (biotin, and handles). The mixture was heated to 70°C and cooled down at a rate of 1°C every 20 min up to 25°C. Half of the DNA origami solution was kept for adding the streptavidin (See the Incorporation of streptavidin to DNA origami section). The other half was later purified by 1% agarose gel electrophoresis run at 70 V for 2 h and stored at 4°C.

4.5 | Incorporation of Streptavidin to DNA Origami

Half of the DNA origami solution from the DNA synthesis was purified from an excess of staples using 100k Amicon filters at 10 000 g for 5 min. Streptavidin was added to the Amicon filtered DNA origami solution to reach an excess of 20-fold and incubated

for 60 min at room temperature. The mix was then purified by 1% agarose gel electrophoresis at 70 V for 2 h and stored at 4°C.

4.6 | Verification of Streptavidin Binding to DNA Origami

A 1.5 nM solution of DNA origami with and without streptavidin and additionally labeled with a single fluorophore (ATTO 647N, shown as a red star in Figure S3a) was incubated for 3 min on a biotin-coated glass substrate. Measurements using Total Internal Reflection Fluorescence (TIRF) microscopy are shown in Figure S3b,c. Fluorescent spots detected over ∼200 video frames were analyzed and summarized in Figure S3d. Since only fluorescence within ∼200 nm from the surface is detectable in TIRF, we conclude that the observed signal comes from the DNA origami binding through biotin-streptavidin interactions, confirming successful functionalization of the DNA with a single streptavidin.

4.7 | Fabrication of the Rh NC Dimers

For the synthesis of Rh NC dimers, T18-functionalized Rh NCs were mixed with the DNA origami solution with a ratio of 20:1 in the TAE buffer containing 12 mM $MgCl_2$ and 600 mM NaCl. The mix was then incubated at room temperature overnight. Obtained structures were then purified by 1% agarose gel electrophoresis run at 70 V for 2 h (Figure S4). The additional band was then extracted from the gel. The obtained structures were used without further purification.

4.8 | Fluorescence Assay of the Rh NC Functionalization

Following the workflow described in Figure 2a, two Rh NCs solutions were prepared as follows: 20 µL of OD15, 19 nm Rh NCs synthesized using the PVP removal protocol. One solution followed the protocol exactly, while in the other, $NaBH_4$ was omitted, keeping all other steps identical. Both solutions were then split in two and mixed with either 10 µL of 5′–AAA AAA AAA AAA AAA AAA–3′ or 5′–CTC TAC CAC CTA CAT–3′, each modified with ATTO 647N at the 5′ end. The four mixtures were diluted in 1x TAE, 12 mM $MgCl_2$ buffer with 0.1% SDS to a final volume of 100 µL. The samples were then incubated for 2 h at room temperature. After incubation, the solutions were centrifuged at 16 000 g for 5 min and pellets were redispersed in 100 µL of 1x TAE, 12 mM $MgCl_2$ with 0.1% SDS. This washing step was repeated three times to remove excess of fluorophore-modified ssDNA. Thus, the only remaining fluorophores in the solution were those attached to the ssDNA hybridized to the Rh-bound strands. Because the fluorophore is quenched when attached to the Rh NCs, it must be released to measure its fluorescence. The melting temperature of the A18–T18 duplex in 12 mM $MgCl_2$ at 10 nM is 45°C (according to the IDT OligoAnalyzer tool); therefore, the solutions were heated to 65°C for 15 min to detach the fluorophores from the Rh NCs. Immediately afterward, all samples were centrifuged at 16 000 g for 5 min at 40°C (the maximum temperature of our centrifuge) and the supernatants were collected for subsequent fluorescence measurements.

After cooling to room temperature, the supernatants collected from the above protocol were transferred into a quartz cuvette and placed in a Duetta spectrometer (HORIBA Scientific). Measurements were performed using the following parameters: excitation wavelength, 647 nm; emission range, 660–900 nm; excitation band pass, 5 nm; emission band pass, 5 nm; integration time, 120 s; detector accumulations, 1; and emission increment, 0.5 nm (1 pixel). To assess the concentration of the DNA on the surface the measurements between 660 and 668 nm were averaged and compared to the fluorescence intensity of known concentration of the fluorophore-labeled DNA strands. The resulting data are shown in Figure 1e.

4.9 | Transmission Electron Microscope

For TEM imaging, 5 µL of the solution were dropped onto EM-Tec Formvar Carbon support film on copper 300 square mesh. After 2 min the solution was removed with a paper filter, and the sample was stained using 2% Uranyl Acetate for 40 sec followed by a quick water rinsing. The measurements were then carried out using a Tecnai Spirit with an accelerating voltage of 120 kV.

4.10 | UV Confocal Setup

The UV microscopy experiments on single DNA origami structures were performed on a custom-built confocal microscope equipped with a LOMO 58×0.8NA water immersion objective. A 266 nm linearly polarized picosecond laser (Picoquant LDH-P-FA-266, 70 ps pulse duration, 80 MHz repetition rate) was used for excitation. The laser beam was spatially filtered with a 50 µm pinhole and spectrally filtered by a short-pass filter (Semrock FF01-311/SP-25). The excitation laser was then reflected toward the sample by a dichroic mirror (Semrock FF310-Di01-25-D). The average 266 nm laser power was 0.22 µW measured before the dichroic mirror at the entrance of the microscope body. A 3-axis piezoelectric stage (Physik Instrumente P-517.3CD) was used to position the sample at the laser focus. The autofluorescence emission in the spectral range of 310–410 nm was collected back by the same microscope objective and separated from the excitation by the dichroic mirror and two emission filters (Semrock FF01-300/LP-25 and Semrock FF01-375/110-25). A 200 mm focal length air-spaced achromatic doublet was used as a microscope tube lens to focus the fluorescence light on a 50 µm confocal pinhole. The autofluorescence light was detected by a single photon photomultiplier tube (Picoquant PMA 175) connected to a time-resolved counting module (Picoquant Picoharp 300 with time-tagged time-resolved mode). The autofluorescence time traces were analysed with the softwares Symphotime64 (Picoquant) and IgorPro (Wavemetrics). All the UV experiments were performed in a freshly prepared 1x TAE buffer at pH 8 with 12 mM $MgCl_2$. The buffer solution was purged with argon for 10 min just before the experiments to remove the dissolved oxygen and reduce the formation of reactive oxygen species.

4.11 | Finite Element Method Simulations

Fluorescence enhancement simulations were performed using the finite element method (FEM) in CST Studio Suite. No adaptive mesh was used. The particles were modeled as cubes with rounded edges of r = 2 nm. The permittivity of water was set to 1.77, and the dielectric function of rhodium was taken from "Handbook of Optical Constants of Solids" by Edward D. Palik. The excitation light was linearly polarized either along or perpendicular to the dimer axis. The fluorescence enhancement factor was calculated by placing a Hertzian dipole at the center of the gap, oriented along the dimer axis. Then enhancement of the quantum yield of the emitter is calculated by:

$$\frac{q}{q_0} = \frac{\frac{\gamma_r}{\gamma_r+\gamma_{loss}+\gamma_{nr}}}{\frac{\gamma_{r0}}{\gamma_{r0}+\gamma_{nr0}}} = \frac{\frac{\frac{\gamma_r}{\gamma_{r0}}}{\frac{\gamma_r+\gamma_{loss}}{\gamma_{r0}}+\frac{\gamma_{nr}}{\gamma_{r0}}}}{q_0} = \frac{\frac{\frac{\gamma_r}{\gamma_{r0}}}{\frac{\gamma_r+\gamma_{loss}}{\gamma_{r0}}+\frac{\gamma_{nr0}}{\gamma_{r0}}}}{q_0}$$
$$= \frac{\frac{\frac{\gamma_r}{\gamma_{r0}}}{\frac{\gamma_r+\gamma_{loss}}{\gamma_{r0}}+\frac{1-q_0}{q_0}}}{q_0} = \frac{\frac{\frac{P_r}{P_{r0}}}{\frac{P_r+P_{loss}}{P_{r0}}+\frac{1-q_0}{q_0}}}{q_0} \quad (1)$$

q = Quantum yield of the emitter in the presence of the NCs

q_0 = Intrinsic quantum yield of the emitter

γ_r = Radiative decay rate of the emitter with NCs

γ_{r0} = Radiative decay rate of the emitter without NCs

γ_{Loss} = Nonradiative decay rate due to energy loss in the NCs

γ_{nr} = Intrinsic nonradiative decay rate of the emitter with NCs

γ_{nr0} = Intrinsic nonradiative decay rate of the emitter without NCs

P_r = Radiated power of the Hertzian dipole with NCs

P_{r0} = Radiated power of the Hertzian dipole without NCs

P_{loss} = Power lost due to absorption in NCs

Thus, the final enhancement factor is equal to $\frac{q}{q_0}\frac{|E|^2}{|E_0|^2}\frac{\eta}{\eta_0}$, where $|E|$ is the magnitude of the electric field at the Hertzian dipole position under irradiation and η is the collection efficiency of our optical setup.

Acknowledgements

G. P. A. and D. G. acknowledge funding from the European Union Program HORIZON-Pathfinder-Open: 3D-BRICKS, grant Agreement 101099125 and from the Swiss State Secretariat for Education, Research and Innovation (SERI) contract number 23.00075. M.K.V., J.W. and D.G. acknowledge funding from the European Research Executive Agency (REA) under the Marie Skłodowska-Curie Actions doctoral network program (Grant Agreement No. 101072818). Y.Y. and Y.Z. acknowledge funding from the U.S. National Science Foundation (Grant No. CHE-1954838).

Open access publishing facilitated by Universite de Fribourg, as part of the Wiley - Universite de Fribourg agreement via the Consortium Of Swiss Academic Libraries.

Conflicts of Interest

The authors declare no conflicts of interest.

Data Availability Statement

The data that support the findings of this study are available from the corresponding author upon reasonable request.

References

1. J. Liu, H. He, D. Xiao, et al., "Recent Advances of Plasmonic Nanoparticles and Their Applications," *Materials* 11, no. 10 (2018): 1833, https://doi.org/10.3390/ma11101833.

2. J. Krajczewski, K. Kołątaj, and A. Kudelski, "Plasmonic Nanoparticles in Chemical Analysis," *RSC Advances* 7, no. 28 (2017): 17559–17576, https://doi.org/10.1039/C7RA01034F.

3. V. E. Bochenkov and T. I. Shabatina, "Chiral Plasmonic Biosensors," *Biosensors* 8, no. 4 (2018): 120, https://doi.org/10.3390/bios8040120.

4. L. Xu, H.-W. Liang, Y. Yang, and S.-H. Yu, "Stability and Reactivity: Positive and Negative Aspects for Nanoparticle Processing," *Chemical Reviews* 118, no. 7 (2018): 3209–3250, https://doi.org/10.1021/acs.chemrev.7b00208.

5. A. Heuer-Jungemann, N. Feliu, I. Bakaimi, et al., "The Role of Ligands in the Chemical Synthesis and Applications of Inorganic Nanoparticles," *Chemical Reviews* 119, no. 8 (2019): 4819–4880, https://doi.org/10.1021/acs.chemrev.8b00733.

6. C. A. Mirkin, R. L. Letsinger, R. C. Mucic, and J. J. Storhoff, "A DNA-Based Method for Rationally Assembling Nanoparticles Into Macroscopic Materials," *Nature* 382, no. 6592 (1996): 607–609, https://doi.org/10.1038/382607a0.

7. A. P. Alivisatos, K. P. Johnsson, X. Peng, et al., "Organization of 'nanocrystal molecules' using DNA," *Nature* 382, no. 6592 (1996): 609–611, https://doi.org/10.1038/382609a0.

8. X. Ma, X. Li, G. Luo, and J. Jiao, "DNA-Functionalized Gold Nanoparticles: Modification, Characterization, and Biomedical Applications," *Frontiers in Chemistry* 10 (2022): 1095488, https://doi.org/10.3389/fchem.2022.1095488.

9. A. Kuzyk, R. Jungmann, G. P. Acuna, and N. Liu, "DNA Origami Route for Nanophotonics," *ACS Photonics* 5, no. 4 (2018): 1151–1163, https://doi.org/10.1021/acsphotonics.7b01580.

10. Y. Dong and Y. Mao, "DNA Origami as Scaffolds for Self-Assembly of Lipids and Proteins," *Chembiochem* 20, no. 19 (2019): 2422–2431, https://doi.org/10.1002/cbic.201900073.

11. M. Dass, F. N. Gür, K. Kołątaj, M. J. Urban, and T. Liedl, "DNA Origami-Enabled Plasmonic Sensing," *The Journal of Physical Chemistry C* 125, no. 11 (2021): 5969–5981, https://doi.org/10.1021/acs.jpcc.0c11238.

12. K. Trofymchuk, K. Kołątaj, V. Glembockyte, et al., "Gold Nanorod DNA Origami Antennas for 3 Orders of Magnitude Fluorescence Enhancement in NIR," *ACS Nano* 17, no. 2 (2023): 1327–1334, https://doi.org/10.1021/acsnano.2c09577.

13. N. Siegel, H. Hasebe, G. Chiarelli, et al., "Universal Click-Chemistry Approach for the DNA Functionalization of Nanoparticles," *Journal of the American Chemical Society* 146, no. 25 (2024): 17250–17260, https://doi.org/10.1021/jacs.4c03833.

14. N. Siegel, M. Sanz-Paz, J. González-Colsa, et al., "Distance-Dependent Interaction Between a Single Emitter and a Single Dielectric Nanoparticle Using DNA Origami," *Small Structures* 6, no. 11 (2025): 2500299, https://doi.org/10.1002/sstr.202500299.

15. J. R. Lakowicz, *Principles of Fluorescence Spectroscopy*. 3rd ed. (Springer, 2006), https://doi.org/10.1007/978-0-387-46312-4.

16. Y. Kumamoto, A. Taguchi, and S. Kawata, "Deep-Ultraviolet Biomolecular Imaging and Analysis," *Advanced Optical Materials* 7, no. 5 (2019): 1801099, https://doi.org/10.1002/adom.201801099.

17. D. Zhao, Z. Lin, W. Zhu, et al., "Recent Advances in Ultraviolet Nanophotonics: From Plasmonics and Metamaterials to Metasurfaces," *Nanophotonics* 10, no. 9 (2021): 2283–2308, https://doi.org/10.1515/nanoph-2021-0083.

18. A. B. T. Ghisaidoobe and S. J. Chung, "Intrinsic Tryptophan Fluorescence in the Detection and Analysis of Proteins: A Focus on Förster Resonance Energy Transfer Techniques," *International Journal of Molecular Sciences* 15, no. 12 (2014): 22518–22538, https://doi.org/10.3390/ijms151222518.

19. I. L. Volkov, Z. V. Reveguk, P. Y. Serdobintsev, R. R. Ramazanov, and A. I. Kononov, "DNA as UV Light–Harvesting Antenna," *Nucleic Acids Research* 46, no. 7 (2018): 3543–3551, https://doi.org/10.1093/nar/gkx1185.

20. A. N. Giordano and R. Rao, "Beyond the Visible: A Review of Ultraviolet Surface-Enhanced Raman Scattering Substrate Compositions, Morphologies, and Performance," *Nanomaterials* 13, no. 15 (2023): 2177, https://doi.org/10.3390/nano13152177.

21. A. Dubey, R. Mishra, C.-W. Cheng, Y.-P. Kuang, S. Gwo, and T.-J. Yen, "Demonstration of a Superior Deep-UV Surface-Enhanced Resonance Raman Scattering (SERRS) Substrate and Single-Base Mutation Detection in Oligonucleotides," *Journal of the American Chemical Society* 143, no. 46 (2021): 19282–19286, https://doi.org/10.1021/jacs.1c09762.

22. V. K. Sharma and H. V. Demir, "Bright Future of Deep-Ultraviolet Photonics: Emerging UVC Chip-Scale Light-Source Technology Platforms, Benchmarking, Challenges, and Outlook for UV Disinfection," *ACS Photonics* 9, no. 5 (2022): 1513–1521, https://doi.org/10.1021/acsphotonics.2c00041.

23. J. O. Arroyo and P. Kukura, "Non-Fluorescent Schemes for Single-Molecule Detection," *Imaging and Spectroscopy Nature Photonics* 10, no. 1 (2016): 11–17, https://doi.org/10.1038/nphoton.2015.251.

24. Q. Li and S. Seeger, "Label-Free Detection of Single Protein Molecules Using Deep UV Fluorescence Lifetime Microscopy," *Analytical Chemistry* 78, no. 8 (2006): 2732–2737, https://doi.org/10.1021/ac052166u.

25. Q. Li and S. Seeger, "Label-Free Detection of Protein Interactions Using Deep UV Fluorescence Lifetime Microscopy," *Analytical Biochemistry* 367, no. 1 (2007): 104–110, https://doi.org/10.1016/j.ab.2007.04.050.

26. M. Lippitz, W. Erker, H. Decker, K. E. V. Holde, and T. Basché, "Two-Photon Excitation Microscopy of Tryptophan-Containing Proteins," *Proceedings of the National Academy of Sciences* 99, no. 5 (2002): 2772–2777, https://doi.org/10.1073/pnas.052662999.

27. B. Sahoo, J. Balaji, S. Nag, S. K. Kaushalya, and S. Maiti, "Protein Aggregation Probed by Two-Photon Fluorescence Correlation Spectroscopy of Native Tryptophan," *The Journal of Chemical Physics* 129, no. 7 (2008): 075103, https://doi.org/10.1063/1.2969110.

28. S. Ranjit, A. Dvornikov, D. A. Holland, G. D. Reinhart, D. M. Jameson, and E. Gratton, "Application of Three-Photon Excitation FCS to the Study of Protein Oligomerization," *The Journal of Physical Chemistry B* 118, no. 50 (2014): 14627–14631, https://doi.org/10.1021/jp511126x.

29. Z. Toprakcioglu, P. Challa, C. Xu, and T. P. J. Knowles, "Label-Free Analysis of Protein Aggregation and Phase Behavior," *ACS Nano* 13, no. 12 (2019): 13940–13948, https://doi.org/10.1021/acsnano.9b05552.

30. A. Barulin, J.-B. Claude, S. Patra, N. Bonod, and J. Wenger, "Deep Ultraviolet Plasmonic Enhancement of Single Protein Autofluorescence in Zero-Mode Waveguides," *Nano Letters* 19, no. 10 (2019): 7434–7442, https://doi.org/10.1021/acs.nanolett.9b03137.

31. A. Barulin, P. Roy, J.-B. Claude, and J. Wenger, "Ultraviolet Optical Horn Antennas for Label-Free Detection of Single Proteins," *Nature Communications* 13, no. 1 (2022): 1842, https://doi.org/10.1038/s41467-022-29546-4.

32. S. K. Jha, Z. Ahmed, M. Agio, Y. Ekinci, and J. F. Löffler, "Deep-UV Surface-Enhanced Resonance Raman Scattering of Adenine on Aluminum Nanoparticle Arrays," *Journal of the American Chemical Society* 134, no. 4 (2012): 1966–1969, https://doi.org/10.1021/ja210446w.

33. B. Sharma, M. F. Cardinal, M. B. Ross, et al., "Aluminum Film-Over-Nanosphere Substrates for Deep-UV Surface-Enhanced Resonance Raman Spectroscopy," *Nano Letters* 16, no. 12 (2016): 7968–7973, https://doi.org/10.1021/acs.nanolett.6b04296.

34. Y. Yang, J. M. Callahan, T.-H. Kim, A. S. Brown, and H. O. Everitt, "Ultraviolet Nanoplasmonics: A Demonstration of Surface-Enhanced Raman Spectroscopy, Fluorescence, and Photodegradation Using Gallium Nanoparticles," *Nano Letters* 13, no. 6 (2013): 2837–2841, https://doi.org/10.1021/nl401145j.

35. Y. Kumamoto, A. Taguchi, M. Honda, K. Watanabe, Y. Saito, and S. Kawata, "Indium for Deep-Ultraviolet Surface-Enhanced Resonance Raman Scattering," *ACS Photonics* 1, no. 7 (2014): 598–603, https://doi.org/10.1021/ph500076k.

36. Y. Zou, L. Mattarozzi, H. Jin, et al., "UV-SERS Monitoring of Plasmonic Photodegradation of Biomolecules on Aluminum Platforms Decorated With Rhodium Nanoparticles," *Nanoscale Advances* 7, no. 17 (2025): 5212–5220, https://doi.org/10.1039/D5NA00486A.

37. P. Ponzellini, G. Giovannini, S. Cattarin, et al., "Metallic Nanoporous Aluminum–Magnesium Alloy for UV-Enhanced Spectroscopy," *The Journal of Physical Chemistry C* 123, no. 33 (2019): 20287–20296, https://doi.org/10.1021/acs.jpcc.9b04230.

38. F. Schuknecht, K. Kołątaj, M. Steinberger, T. Liedl, and T. Lohmueller, "Accessible Hotspots for Single-Protein SERS in DNA-Origami Assembled Gold Nanorod Dimers With Tip-to-Tip Alignment," *Nature Communications* 14, no. 1 (2023): 7192, https://doi.org/10.1038/s41467-023-42943-7.

39. G. P. Acuna, F. M. Möller, P. Holzmeister, S. Beater, B. Lalkens, and P. Tinnefeld, "Fluorescence Enhancement at Docking Sites of DNA-Directed Self-Assembled Nanoantennas," *Science* 338, no. 6106 (2012): 506–510, https://doi.org/10.1126/science.1228638.

40. I. Kaminska, J. Bohlen, S. Mackowski, P. Tinnefeld, and G. P. Acuna, "Strong Plasmonic Enhancement of a Single Peridinin–Chlorophyll a – Protein Complex on DNA Origami-Based Optical Antennas," *ACS Nano* 12, no. 2 (2018): 1650–1655, https://doi.org/10.1021/acsnano.7b08233.

41. S. Tian, O. Neumann, M. J. McClain, et al., "Aluminum Nanocrystals: A Sustainable Substrate for Quantitative SERS-Based DNA Detection," *Nano Letters* 17, no. 8 (2017): 5071–5077, https://doi.org/10.1021/acs.nanolett.7b02338.

42. M. H. Chowdhury, K. Ray, S. K. Gray, J. Pond, and J. R. Lakowicz, "Aluminum Nanoparticles as Substrates for Metal-Enhanced Fluorescence in the Ultraviolet for the Label-Free Detection of Biomolecules," *Analytical Chemistry* 81, no. 4 (2009): 1397–1403, https://doi.org/10.1021/ac802118s.

43. K. Ray, H. Szmacinski, and J. R. Lakowicz, "Enhanced Fluorescence of Proteins and Label-Free Bioassays Using Aluminum Nanostructures," *Analytical Chemistry* 81, no. 15 (2009): 6049–6054, https://doi.org/10.1021/ac900263k.

44. S. K. Jha, N. Mojarad, M. Agio, J. F. Löffler, and Y. Ekinci, "Enhancement of the Intrinsic Fluorescence of Adenine Using Aluminum Nanoparticle Arrays," *Optics Express* 23, no. 19 (2015): 24719–24729, https://doi.org/10.1364/OE.23.024719.

45. A. Ono, M. Kikawada, R. Akimoto, W. Inami, and Y. Kawata, "Fluorescence Enhancement With Deep-Ultraviolet Surface Plasmon Excitation," *Optics Express* 21, no. 15 (2013): 17447–17453, https://doi.org/10.1364/OE.21.017447.

46. L. Li, S. Fang Lim, A. A. Puretzky, R. Riehn, and H. D. Hallen, "Near-Field Enhanced Ultraviolet Resonance Raman Spectroscopy Using

Aluminum Bow-Tie Nano-Antenna," *Applied Physics Letters* 101, no. 11 (2012): 113116, https://doi.org/10.1063/1.4746747.

47. P. Roy, J.-B. Claude, S. Tiwari, A. Barulin, and J. Wenger, "Ultraviolet Nanophotonics Enables Autofluorescence Correlation Spectroscopy on Label-Free Proteins With a Single Tryptophan," *Nano Letters* 23, no. 2 (2023): 497–504, https://doi.org/10.1021/acs.nanolett.2c03797.

48. P. Roy, S. Zhu, J.-B. Claude, J. Liu, and J. Wenger, "Ultraviolet Resonant Nanogap Antennas With Rhodium Nanocube Dimers for Enhancing Protein Intrinsic Autofluorescence," *ACS Nano* 17, no. 22 (2023): 22418–22429, https://doi.org/10.1021/acsnano.3c05008.

49. J. M. Sanz, D. Ortiz, R. Alcaraz de la Osa, et al., "UV Plasmonic Behavior of Various Metal Nanoparticles in the Near- and Far-Field Regimes: Geometry and Substrate Effects," *The Journal of Physical Chemistry C* 117, no. 38 (2013): 19606–19615, https://doi.org/10.1021/jp405773p.

50. Y. Gutiérrez, R. Alcaraz de la Osa, D. Ortiz, J. M. Saiz, F. González, and F. Moreno, "Plasmonics in the Ultraviolet With Aluminum, Gallium, Magnesium and Rhodium," *Applied Sciences* 8, no. 1 (2018): 64, https://doi.org/10.3390/app8010064.

51. J. M. McMahon, G. C. Schatz, and S. K. Gray, "Plasmonics in the Ultraviolet With the poor metals Al, Ga, In, Sn, Tl, Pb, and Bi," *Physical Chemistry Chemical Physics* 15, no. 15 (2013): 5415–5423, https://doi.org/10.1039/C3CP43856B.

52. M. B. Ross and G. C. Schatz, "Aluminum and Indium Plasmonic Nanoantennas in the Ultraviolet," *The Journal of Physical Chemistry C* 118, no. 23 (2014): 12506–12514, https://doi.org/10.1021/jp503323u.

53. D. Renard, S. Tian, M. Lou, et al., "UV-Resonant Al Nanocrystals: Synthesis, Silica Coating, and Broadband Photothermal Response," *Nano Letters* 21, no. 1 (2021): 536–542, https://doi.org/10.1021/acs.nanolett.0c04020.

54. B. D. Clark, C. R. Jacobson, M. Lou, et al., "Aluminum Nanocubes Have Sharp Corners," *ACS Nano* 13, no. 8 (2019): 9682–9691, https://doi.org/10.1021/acsnano.9b05277.

55. M. Yarema, M. Wörle, M. D. Rossell, et al., "Monodisperse Colloidal Gallium Nanoparticles: Synthesis, Low Temperature Crystallization, Surface Plasmon Resonance and Li-Ion Storage," *Journal of the American Chemical Society* 136, no. 35 (2014): 12422–12430, https://doi.org/10.1021/ja506712d.

56. E. R. Hopper, T. M. R. Wayman, J. Asselin, et al., "Size Control in the Colloidal Synthesis of Plasmonic Magnesium Nanoparticles," *The Journal of Physical Chemistry C* 126, no. 1 (2022): 563–577, https://doi.org/10.1021/acs.jpcc.1c07544.

57. D. Renard, S. Tian, A. Ahmadivand, et al., "Polydopamine-Stabilized Aluminum Nanocrystals: Aqueous Stability and Benzo[a]Pyrene Detection," *ACS Nano* 13, no. 3 (2019): 3117–3124, https://doi.org/10.1021/acsnano.8b08445.

58. P. Roy, C. Badie, J.-B. Claude, et al., "Preventing Corrosion of Aluminum Metal With Nanometer-Thick Films of Al_2O_3 Capped With TiO_2 for Ultraviolet Plasmonics," *ACS Applied Nano Materials* 4, no. 7 (2021): 7199–7205, https://doi.org/10.1021/acsanm.1c01160.

59. E. Cortés, F. J. Wendisch, L. Sortino, et al., "Optical Metasurfaces for Energy Conversion," *Chemical Reviews* 122, no. 19 (2022): 15082–15176, https://doi.org/10.1021/acs.chemrev.2c00078.

60. J. L. Montaño-Priede, O. Peña-Rodríguez, and U. Pal, "Near-Electric-Field Tuned Plasmonic Au@SiO_2 and Ag@SiO_2 Nanoparticles for Efficient Utilization in Luminescence Enhancement and Surface-Enhanced Spectroscopy," *The Journal of Physical Chemistry C* 121, no. 41 (2017): 23062–23071, https://doi.org/10.1021/acs.jpcc.7b07395.

61. L. Xu, D. Liu, D. Chen, H. Liu, and J. Yang, "Size and Shape Controlled Synthesis of Rhodium Nanoparticles," *Heliyon* 5, no. 1 (2019): e01165, https://doi.org/10.1016/j.heliyon.2019.e01165.

62. A. M. Watson, X. Zhang, R. Alcaraz de la Osa, et al., "Rhodium Nanoparticles for Ultraviolet Plasmonics," *Nano Letters* 15, no. 2 (2015): 1095–1100, https://doi.org/10.1021/nl5040623.

63. X. Zhang, P. Li, Á. Barreda, et al., "Size-Tunable Rhodium Nanostructures for Wavelength-Tunable Ultraviolet Plasmonics," *Nanoscale Horizons* 1, no. 1 (2015): 75–80, https://doi.org/10.1039/C5NH00062A.

64. R. A. Osa, J. M. Sanz, A. I. Barreda, et al., "Rhodium Tripod Stars for UV Plasmonics," *Journal of Physical Chemistry C* 119, no. 22 (2015): 12572–12580, https://doi.org/10.1021/acs.jpcc.5b00983.

65. D. M. Arboleda, V. Coviello, A. Palumbo, R. Pilot, and V. Amendola, "Rhodium Nanospheres for Ultraviolet and Visible Plasmonics," *Nanoscale Horizons* 10, no. 2 (2025): 336–348, https://doi.org/10.1039/D4NH00449C.

66. Y. Xie, Q. Wu, C. Zhou, et al., "Rhodium Ultraviolet Plasmonic Nanocavities With Narrow Plasmon-Induced Reflection and Polarization-Tunable Field Enhancement for High-Performance SERS and Sensing," *Optics Express* 33, no. 14 (2025): 30648–30659, https://doi.org/10.1364/OE.566961.

67. D. S. White, M. A. Smith, B. Chanda, and R. H. Goldsmith, "Strategies for Overcoming the Single-Molecule Concentration Barrier," *ACS Measurement Science Au* 3 (2023): 239–257, https://doi.org/10.1021/acsmeasuresciau.3c00002.

68. T. Roesel, A. Dahlin, M. Piliarik, L. W. Fitzpatrick, and B. Špačková, "Label-Free Single-Molecule Optical Detection," *npj Biosensing* 2, no. 1 (2025): 32, https://doi.org/10.1038/s44328-025-00048-9.

69. B. Liu and J. Liu, "Freezing Directed Construction of Bio/Nano Interfaces: Reagentless Conjugation, Denser Spherical Nucleic Acids, and Better Nanoflares," *Journal of the American Chemical Society* 139, no. 28 (2017): 9471–9474, https://doi.org/10.1021/jacs.7b04885.

70. F. Lu, Y. Tian, M. Liu, et al., "Discrete Nanocubes as Plasmonic Reporters of Molecular Chirality," *Nano Letters* 13, no. 7 (2013): 3145–3151, https://doi.org/10.1021/nl401107g.

71. A. K. Adamczyk, T. A. P. M. Huijben, M. Sison, et al., "DNA Self-Assembly of Single Molecules With Deterministic Position and Orientation," *ACS Nano* 16, no. 10 (2022): 16924–16931, https://doi.org/10.1021/acsnano.2c06936.

72. K. Trofymchuk, V. Glembockyte, L. Grabenhorst, et al., "Addressable Nanoantennas With Cleared Hotspots for Single-Molecule Detection on a Portable Smartphone Microscope," *Nature Communications* 12, no. 1 (2021): 950, https://doi.org/10.1038/s41467-021-21238-9.

73. J. R. Lakowicz, "Radiative Decay Engineering 3. Surface Plasmon-Coupled Directional Emission," *Analytical Biochemistry* 324, no. 2 (2004): 153–169, https://doi.org/10.1016/j.ab.2003.09.039.

74. Construction of Nanoparticle-on-Mirror Nanocavities and Their Applications in Plasmon-Enhanced Spectroscopy. *Chemical Science* 2024, 15 (8), 2697–2711, https://doi.org/10.1039/d3sc05722d.

75. Y. Zou, N. Corduri, F. DAmico, et al., "Sel-Assembled Rhodium Nanoantennas for Single-Protein UV SERS," *arXiv* (2026), https://doi.org/10.48550/arXiv.2601.13043.

76. R. F. Chen, "Fluorescence Quantum Yields of Tryptophan and Tyrosine," *Analytical Letters* 1, no. 1 (1967): 35–42, https://doi.org/10.1080/00032716708051097.

77. C. Sikeler, F. Haslinger, I. V. Martynenko, and T. Liedl, "DNA Origami-Directed Self-Assembly of Gold Nanospheres for Plasmonic Metasurfaces," *Advanced Functional Materials* 34, no. 42 (2024): 2404766, https://doi.org/10.1002/adfm.202404766.

78. J. M. Eeftens, J. van der Torre, D. R. Burnham, and C. Dekker, "Copper-Free Click Chemistry for Attachment of Biomolecules in Magnetic Tweezers," *BMC Biophysics* 8 (2015): 9, https://doi.org/10.1186/s13628-015-0023-9.

79. J. de Torres, M. Mivelle, S. B. Moparthi, et al., "Plasmonic Nanoantennas Enable Forbidden Förster Dipole–Dipole Energy Transfer and Enhance the FRET Efficiency," *Nano Letters* 16, no. 10 (2016): 6222–6230, https://doi.org/10.1021/acs.nanolett.6b02470.

80. S. Bidault, A. Devilez, P. Ghenuche, B. Stout, N. Bonod, and J. Wenger, "Competition Between Förster Resonance Energy Transfer and Donor

Photodynamics in Plasmonic Dimer Nanoantennas," *ACS Photonics* 3, no. 5 (2016): 895–903, https://doi.org/10.1021/acsphotonics.6b00148.

81. J. V. Pellegrotti, G. P. Acuna, A. Puchkova, et al., "Controlled Reduction of Photobleaching in DNA Origami–Gold Nanoparticle Hybrids," *Nano Letters* 14, no. 5 (2014): 2831–2836, https://doi.org/10.1021/nl500841n.

82. S. Patra, J.-B. Claude, and J. Wenger, "Fluorescence Brightness, Photostability, and Energy Transfer Enhancement of Immobilized Single Molecules in Zero-Mode Waveguide Nanoapertures," *ACS Photonics* 9, no. 6 (2022): 2109–2118, https://doi.org/10.1021/acsphotonics.2c00349.

83. J. P. Hoogenboom, J. Hernando, E. M. H. P. van Dijk, N. F. van Hulst, and M. F. García-Parajó, "Power-Law Blinking in the Fluorescence of Single Organic Molecules," *Chemphyschem* 8, no. 6 (2007): 823–833, https://doi.org/10.1002/cphc.200600783.

84. T. Hirschfeld, "Quantum Efficiency Independence of the Time Integrated Emission From a Fluorescent Molecule," *Applied Optics* 15, no. 12 (1976): 3135–3139, https://doi.org/10.1364/AO.15.003135.

85. C. Eggeling, A. Volkmer, and C. A. M. Seidel, "Molecular Photobleaching Kinetics of Rhodamine 6G by One- and Two-Photon Induced Confocal Fluorescence Microscopy," *Chemphyschem* 6, no. 5 (2005): 791–804, https://doi.org/10.1002/cphc.200400509.

86. X. Zhang, B. Liu, C. Hu, et al., "A Facile Method in Removal of PVP Ligands From Silver Nanowires for High Performance and Reusable SERS Substrate," *Spectrochimica Acta Part A: Molecular and Biomolecular Spectroscopy* 228 (2020): 117733, https://doi.org/10.1016/j.saa.2019.117733.

Supporting Information

Additional supporting information can be found online in the Supporting Information section.

Supporting File: adfm74946-sup-0001-SuppMat.docx.